ACS APPLIED MATERIALS & INTERFACES

Research Article

www.acsami.org

Improved Performance and Stability of Inverted Planar Perovskite Solar Cells Using Fulleropyrrolidine Layers

Chengbo Tian,[†,§] Edison Castro,[†,§] Tan Wang,[‡] German Betancourt-Solis,[†] Gloria Rodriguez,[†] and Luis Echegoyen*[,†]

[†]Department of Chemistry, University of Texas at El Paso, 500 West University Avenue, El Paso, Texas 79968, United States

[‡]iChEM (Collaborative Innovation Center of Chemistry for Energy Materials), Department of Chemistry, College of Chemistry and Chemical Engineering, Xiamen University, Xiamen 361005, China

Supporting Information

ABSTRACT: Inverted planar structure perovskite solar cells (PSCs), due to their low-temperature precessing and lack of hysteretic problems, are attracting increased attention by researchers around the world. Fullerene derivatives are the most widely used electron transport materials (ETMs) in inverted planar perovskite solar cells, especially [6,6]-phenyl-C_{61}-butyric acid methylester ($PC_{61}BM$), which exhibits very good performance. However, to the best of our knowledge, the influence of adducts on fullerene-based PSCs performance has not been fully explored to date. In this work, two fullerene derivatives, 2,5-(dimethyl ester) C_{60} fulleropyrrolidine ($DMEC_{60}$) and the analogous C_{70} derivative ($DMEC_{70}$), were synthesized in high yield via a 1,3-dipolar cycloaddition reaction at room temperature and incorporated into $CH_3NH_3PbI_3$ perovskite solar cells as electron transport materials. Possibly because the attached pyrrolidine ester groups are able to coordinate with the perovskite layer, the devices based on $DMEC_{60}$ and $DMEC_{70}$ achieved power conversion efficiencies (PCE) of 15.2% and 16.4%, respectively. Not only were both devices' efficiencies higher than those based on $PC_{61}BM$ and $PC_{71}BM$, but their stabilities were also higher than those for PCBM-based devices. The results suggest that $DMEC_{60}$ and $DMEC_{70}$ are better alternatives than $PC_{61}BM$ and $PC_{71}BM$ for the ETMs in PSCs.

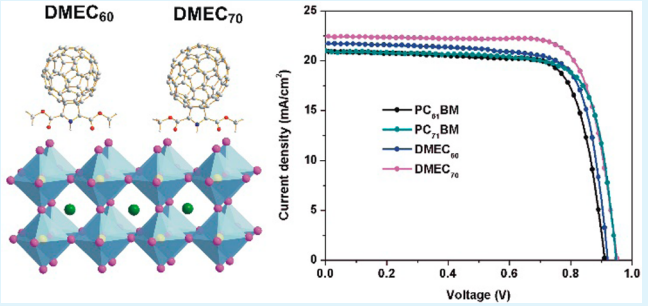

KEYWORDS: *perovskite solar cells, fullerene derivatives, electron transport layer, interfacial interactions, coordination*

1. INTRODUCTION

The unique properties of organic−inorganic hybrid perovskite materials make them promising candidates for developing next-generation photovoltaic cells for commercial applications to compete with silicon solar cells.[1−5] Perovskite solar cells (PSCs) based on such materials have shown a remarkable increase from 3.8% in 2009 to 22.1% in 2016.[1,6−14]

In an effort to meet commercial demand, the inverted planar structure PSCs with the configuration substrate/PEDOT−PSS/perovskite/fullerene derivative have recently attracted more attention due to their simple structure, low-temperature processing and negligible hysteric behavior.[15] For the hole-transporting material (HTM), besides PEDOT−PSS, NiO_x, and CuI have also been reported by some research groups.[8,16−20] However, the good electron transporting and solution processable properties of most fullerene derivatives have made them the most popular ETMs in PSCs.[15,21]

In 2013, Guo and co-workers first tried $PC_{61}BM$ as the ETM in inverted planar PSCs and obtained a PCE of 3.9%. This result suggested that $PC_{61}BM$ can work as a relatively efficient ETM in PSCs.[16] In 2014, Lam et al. reported an efficiency of 7.4% for PSCs using $PC_{61}BM$ as the ETM after optimizing the conditions for the preparation of the perovskite layers.[22] Nie and Im's group, by further optimization of the conditions of perovskite deposition, obtained even higher PCEs, as high as 18%.[23,24]

Besides $PC_{61}BM$, several studies have shown that other fullerene derivatives or unique double fullerene layers can also work as efficient ETLs in PSCs. Wu and co-workers reported a device with a PCE of 16.3% by employing $PC_{71}BM$ as the ETM, in which a solvent-annealing procedure was utilized.[25] To further optimize the PSCs' performance, Jen's and Huang's groups, among others, have reported using different double fullerene layers (consisting of $PC_{61}BM/C_{60}$, ICBA/C_{60}, C_{60}/bis-C_{60}, etc.) as the interface layer to get high effiencies.[15,26−32] Meanwhile, conjugated polymer electrolytes and inorganic oxide materials have also been developed as efficient interfacial materials with a $PC_{61}BM$ layer by Snaith and others.[17,33−36] These results demonstrate that fullerenes or fullerene derivatives are excellent ETMs for high-performance PSCs.

Received: August 24, 2016
Accepted: October 21, 2016
Published: October 21, 2016

DOI: 10.1021/acsami.6b10668
ACS Appl. Mater. Interfaces 2016, 8, 31426−31432

Scheme 1. Synthesis of $DMEC_{60}$ and $DMEC_{70}$

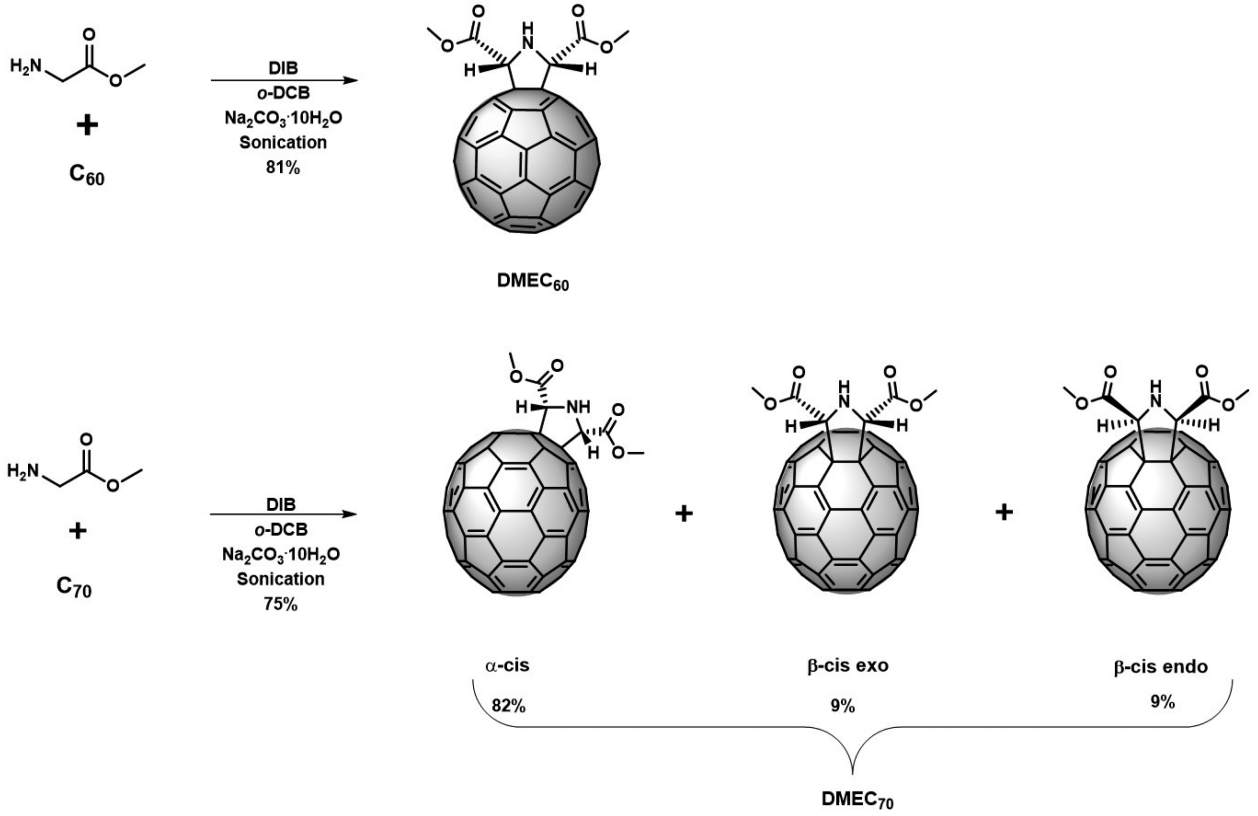

However, the influence of the functional groups on the fullerene-based PSCs has not been systematically probed.[27,30] Therefore, designing novel structures of fullerene derivatives to probe the fundamental principles that underlie their structure–perovskite performance is of utmost importance.

Here, we report the design and synthesis of two pyrrolidine ester functionalized fullerene derivatives, $DMEC_{60}$ and $DMEC_{70}$, and their performance as the ETMs in PSCs. The best efficiencies obtained for the devices based on $DMEC_{60}$ and $DMEC_{70}$ were found to be 15.2% and 16.5%, respectively. These values were higher than those obtained for the corresponding $PC_{61}BM$- and $PC_{71}BM$-based PSCs, 14.5% and 15.0%, respectively. We propose that specific binding of these fullerene derivatives with the perovskite layer surface can not only effectively enhance the electron extraction efficiency but also increase the stability of the corresponding devices.

2. EXPERIMENTAL SECTION

2.1. Materials Synthesis. $DMEC_{60}$ was synthesized following a reported procedure,[37] and $DMEC_{70}$ was synthesized following the same procedure (Scheme 1). The ^1H NMR of $DMEC_{70}$ shows signals for the amino group at 3.55, 3.44, and 3.23 ppm, which indicates the presence of three isomers. The ratio of the monoadducts in the mixture was 82:9:9 (α–β_{endo}–β_{exo}), respectively, as determined by ^1H NMR (Figure S5), and the molecular mass was determined by matrix assisted laser desorption ionization time-of-flight mass spectrometry (MALDI-TOF-MS) (Figure S4).

2.2. Device Fabrication. $PC_{61}BM$ (99%) and $PC_{71}BM$ (99%) were bought from Nano-C. The purity of $DMEC_{60}$ and $DMEC_{70}$ was determined using NMR (>99%). Methylammonium iodide (CH_3NH_3I) was synthesized using a previously reported method.[9] Perovskite solar cells with the configuration FTO/PEDOT–PSS (40 nm)/$CH_3NH_3PbI_3$ (330 nm)/$PC_{61}BM$ ($PC_{71}BM$, $DMEC_{60}$, or $DMEC_{70}$ fullerene derivatives) (100 nm)/LiF (0.5 nm)/Al (100 nm) were fabricated on FTO-coated glass substrates with a resistivity of 10 Ω/cm^2. Prior to fabrication, the patterned FTO glass substrates were cleaned sequentially with detergent, deionized water, acetone, and isopropanol 10 min for each step. Next, the FTO glass substrates were dried with nitrogen gas and treated in a UV–ozone oven for 30 min. After passing through a 0.45 μm PVDF filter, the PEDOT–PSS solution (Baytron P VP AI 4083) was spin-coated onto the cleaned FTO substrates at 5000 rpm for 30 s and baked at 150 °C for 15 min in air. Next, a solution of 1 M PbI_2 in DMF was spin-coated at 3000 rpm for 30 s on top of the prepared substrates and dried on a hot plate at 70 °C for 10 min. Then, the FTO/PEDOT–PSS/PbI_2 substrates were transferred into a vacuum oven for conversion to $CH_3NH_3PbI_3$ by a vapor-assisted gas–solid crystallization process following previously reported methods.[20,44] After the $CH_3NH_3PbI_3$ films were formed and then cooled to room temperature, 2 wt % $PC_{61}BM$ ($PC_{71}BM$, $DMEC_{60}$ or $DMEC_{70}$) dissolved in chlorobenzene was spin-coated onto the $CH_3NH_3PbI_3$ layer at 1200 rpm for 30 s. To complete the devices, LiF (0.5 nm) and Al electrode (100 nm) were deposited by thermal evaporation under a pressure of 2×10^{-6} Torr through a shadow mask. The active area of the devices was 7 mm^2.

2.3. Device Characterization. The J–V characteristics of the photovoltaic cells were recorded using a Keithley 2420 source measure unit under a Photo Emission Tech SS100 Solar Simulator, and the light intensity was calibrated by a standard Si solar cell. The external quantum efficiency (EQE) was measured using a Bentham (Bentham Instruments Ltd.) measurement system. The light intensity was calibrated using a single-crystal Si photovoltaic cell as the reference. The J–V and EQE measurements were carried out in air. The scanning electron microscopy (SEM) images were taken on a ZEISS Sigma FE-SEM. The SEM images were collected by using a ZEISS Sigma FE-SEM, in which the electron beam was accelerated in the range of 500 V to 30 kV. The X-ray diffraction (XRD) patterns were recorded on a Bruker X-ray diffraction instrument using Cu Kα radiation. Film thicknesses were measured using a KLA Tencor profilometer. Time-resolved photoluminescence (TRPL) was analyzed using an Edinburgh instruments FLS980 fluorescence spectrometer.

DOI: 10.1021/acsami.6b10668
ACS Appl. Mater. Interfaces 2016, 8, 31426–31432

3. RESULTS AND DISCUSSION

The synthetic method followed to prepare $DMEC_{60}$ and $DMEC_{70}$ is presented in Scheme 1. These two fullerene derivatives were synthesized by a 1,3-dipolar cycloaddition reaction using a modified procedure from previous work.[37] Detailed synthetic procedures and charaterizations are described in the Experimental section and the Supporting Information. The two ester groups enhance the solubility of the fullerene derivatives and improve solution processing during device fabrication.

To assess the potential implementation of $DMEC_{60}$ and $DMEC_{70}$ as the ETMs for PCSs, the electrochemical and optical properties of $DMEC_{60}$ and $DMEC_{70}$ were analyzed by cyclic voltammetry (CV) and UV−vis absorption spectroscopy. As shown in Figure 1a, both of the compounds exhibit three

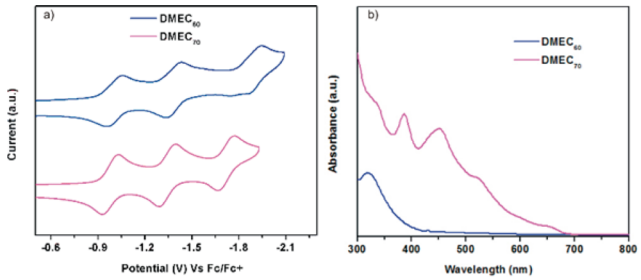

Figure 1. (a) Cyclic voltammetric results for $DMEC_{60}$ and $DMEC_{70}$ at a scan rate of 100 mV/s. (b) UV−vis absorption spectra of $DMEC_{60}$ and $DMEC_{70}$ in toluene solution.

reversible reduction waves in the potential range between 0 and −2.0 V versus Fc−Fc^+. The energy of the lowest unoccupied molecular orbital (LUMO) level was estimated from their onset reduction potentials (E_{red}^{on}) and an equation (LUMO energy = $-e(E_{red}^{on} + 4.80; eV)$),[38] and the values are listed in Table 1. The

Table 1. Electrochemical and Photophysical Data of $DMEC_{60}$ and $DMEC_{70}$

compound	λ_{abs} (nm)	E_g (eV)	E_{red}^{on} (V)	LUMO (eV)	HOMO (eV)
$DMEC_{60}$	714	1.74	0.89	3.89	5.63
$DMEC_{70}$	683	1.81	0.90	3.90	5.71

LUMO energy levels were estimated at −3.91 eV and −3.90 eV, respectively, which are identical to that of $PC_{61}BM$ and $PC_{71}BM$ (−3.91 eV).[39] In agreement with previous literature and our experimental data,[26,40,41] the LUMO energy levels of $DMEC_{60}$ and $DMEC_{70}$ suggest that both compounds could serve as effective ETMs in PSCs.

The absorption spectra of $DMEC_{60}$ and $DMEC_{70}$ in toluene solution at room temperature are shown in Figure 1b. Both exhibit strong UV absorption from 300 to 400 nm. The absorptions of $DMEC_{60}$ and $PC_{61}BM$ are very similar over the whole region. The absorptions of $DMEC_{70}$ are much stronger than that of $DMEC_{60}$ due to the extended conjugated structure. From the absorption onset of $DMEC_{60}$ and $DMEC_{70}$, we can readily obtain the band gap for them. Combined with the electrochemical results, they allow the determination of the HOMO energy levels of these two compounds (Table 1).

The electron mobility of $DMEC_{60}$ and $DMEC_{70}$ based on electron-only devices was evaluated by the space-charge limited current (SCLC) method and the Mott−Gurney law,[42] as shown in Figure S8. Using this method, values of 7.21×10^{-4} and 9.07×10^{-4} cm^2 V^{-1} s^{-1} were obtained for $DMEC_{60}$ and $DMEC_{70}$, respectively, which are very close to the values from $PC_{61}BM$ and $PC_{71}BM$ (6.85×10^{-4} cm^2 V^{-1} s^{-1} and 9.19×10^{-4} cm^2 V^{-1} s^{-1}, respectively). On the basis of these relative values, both $DMEC_{60}$ and $DMEC_{70}$ are good candidates for ETMs.[43,44]

To evaluate the performance of $DMEC_{60}$ and $DMEC_{70}$ as the ETM in PSCs, devices with a configuration of FTO/PEDOT−PSS/$CH_3NH_3PbI_3$/$PC_{61}BM$ ($PC_{71}BM$, $DMEC_{60}$ or $DMEC_{70}$)/LiF/Al were fabricated. From the values in Table 1 and from previous reports, the energy-level alignment is shown in Figure 2a. Because the LUMO energy level of $CH_3NH_3PbI_3$ is −3.9 eV, the values are sufficient for electron extraction from the perovskite to the fullerene derivative layer.

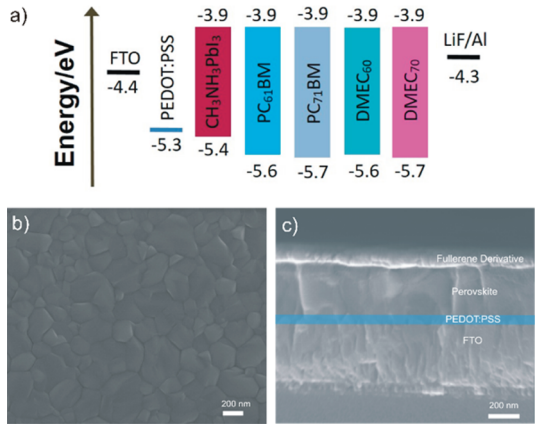

Figure 2. (a) Energy-level diagram of the materials used in the PSCs. (b) Top-view SEM image of the perovskite film. (c) Cross-sectional SEM image of the device FTO/PEDOT−PSS/perovskite/fullerene derivative film.

The device preparation process was similar to that reported in previous reports.[20,45] The morphology of the perovskite layer was studied by scanning electron microscopy (SEM). As shown in Figure 2b, the perovskite films, which were formed on the PEDOT−PSS layers exhibit full surface coverage and uniform microscale grain structure with no pinholes.

Additionally, the cross-section shown in Figure 2c allows the clear observation of all of the layers. An extremely uniform and thick perovskite layer (ca. 330 nm) was obtained on the PEDOT−PSS layer. The results from Figure 2b,c clearly show that the microscale and homogeneous grains of the perovskite layer should allow very good contact with the ETM layer, thus efficiently decreasing the grain boundary energy. This suggests that the perovskite films prepared using this procedure should lead to high-efficiency PSCs. The perovskite layer was also analyzed by X-ray diffraction (XRD). As shown in Figure S9, the diffraction peaks were located at 2θ values of 14.19, 20.09, 23.57, 24.56, 28.49, 31.95, 35.19, 40.69, and 50.29, corresponding to planes (110), (112), (211), (202), (220), (310), (312), (224), and (404) of the perovskite tetragonal structure,[46−48] which indicates that the PbI_2 layer was fully converted into the perovskite layer.

The current−voltage (J−V) characteristics of PSCs using $PC_{61}BM$, $PC_{71}BM$, $DMEC_{60}$, and $DMEC_{70}$ as the ETMs were tested under AM 1.5G irradiation (100 mW cm^{-2}). The best performances of the cells are shown in Figure 3 and the key photovoltaic performance parameters of V_{oc}, J_{sc}, FF, and PCE of the devices are listed in Table 2. The best devices employing

DOI: 10.1021/acsami.6b10668
ACS Appl. Mater. Interfaces 2016, 8, 31426−31432

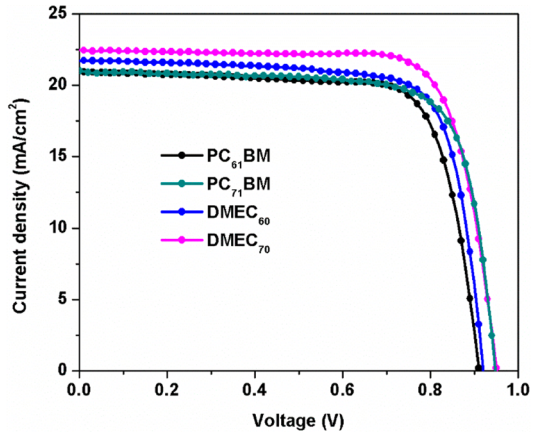

Figure 3. J–V curves for perovskite solar cells fabricated by using $DMEC_{60}$ and $DMEC_{70}$ as ETMs and reference cells with $PC_{61}BM$ and $PC_{71}BM$ ETMs.

Table 2. Summary of the Device Performance Analysis in Figure 3 (Calculated J_{sc} Values Obtained from EQE Results)

type	V_{oc} (V)	J_{sc} (mA/cm^2)	calculated J_{sc} (mA/cm^2)	FF (%)	PCE (%)
$PC_{61}BM$	0.91	20.92	20.1	76.0	14.5
$PC_{71}BM$	0.95	21.03	20.3	75.5	15.1
$DMEC_{60}$	0.92	21.73	20.5	75.8	15.2
$DMEC_{70}$	0.95	22.44	21.3	77.1	16.4

$DMEC_{60}$ and $DMEC_{70}$ as ETMs resulted in PCEs of 15.2% and 16.4%, respectively. The efficiencies are not only significantly higher than that of the devices with $PC_{61}BM$ as ETM, which yielded a PCE of 14.5% under the same conditions, but also higher than that of $PC_{71}BM$-based devices (15.1%).

As shown in Figure 4, a histogram of the PCEs of 30 individual devices based on $PC_{61}BM$, $PC_{71}BM$, $DMEC_{60}$, and $DMEC_{70}$ as the ETLs are presented with average efficiencies of 13.5 ± 0.9%, 14.0 ± 1.2%, 14.1 ± 1.1%, and 15.2 ± 1.2%,

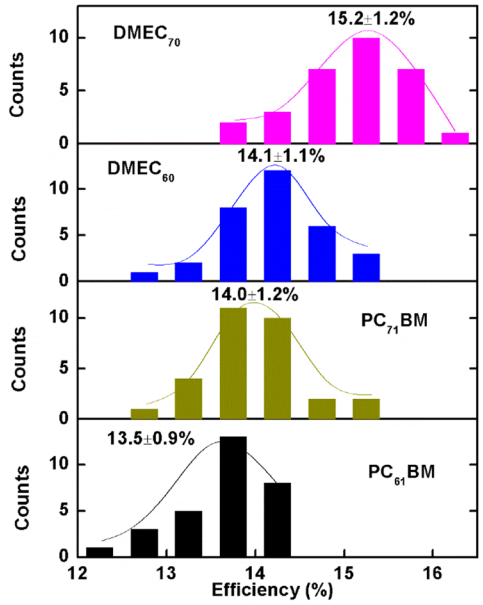

Figure 4. Histograms of device PCE measured for 30 individual devices based on $PC_{61}BM$, $PC_{71}BM$, $DMEC_{60}$, and $DMEC_{70}$ ETMs.

respectively. The statistical diagram of the values of J_{sc}, V_{oc}, and FF for the devices with different fullerene derivatives is shown in Figure S10, and the average of these values is presented in Table 2.

Compared with the $PC_{61}BM$- and $DMEC_{60}$-based devices, the $PC_{71}BM$- and $DMEC_{70}$-based devices displayed a slightly higher V_{oc}. On the basis of previous reports, the higher V_{oc} could be attributed to the higher electron mobility of $PC_{71}BM$ and $DMEC_{70}$ compared with those of $PC_{61}BM$ or $DMEC_{60}$ because the high electron mobility can effectively reduce charge recombination at the perovskite–fullerene interface and minimize potential losses across this interface.[27]

In addition, the J_{sc} data of the devices involving $DMEC_{60}$ and $DMEC_{70}$ (21.73 and 22.44 mA cm^{-2} for $DMEC_{60}$ and $DMEC_{70}$, respectively) are higher than those of $PC_{61}BM$ (20.92 mA cm^{-2}) and $PC_{71}BM$ (21.03 mA cm^{-2}). The J_{sc} of $PC_{61}BM$-, $PC_{71}BM$-, $DMEC_{60}$-, and $DMEC_{70}$-based devices can be verified by their external quantum efficiency spectra. As shown in Figure S11, the EQE spectra of perovskite solar cells using $PC_{61}BM$, $PC_{71}BM$, $DMEC_{60}$, or $DMEC_{70}$ as the ETMs were measured by IPCE measurements. The integrated current densities from the EQE spectra for devices using $PC_{61}BM$, $PC_{71}BM$, $DMEC_{60}$, and $DMEC_{70}$ as ETMs are 20.1, 20.3, 20.5, and 21.3 mA cm^{-2}, respectively, which is in accordance with the corresponding J_{sc} values obtained from the J–V curves, with differences within 5%. In view of the very similar film quality of the perovskite layers for all fullerene ETMs, we speculate that the increase in J_{sc} could be due to two possible reasons.

According to previous reports,[49] the ETM in PSCs usually plays two roles: to extract electrons from the perovskite and to transport electrons to the cathode. As discussed above, $DMEC_{60}$ and $DMEC_{70}$ have similar electron transporting abilities to those of $PC_{61}BM$ and $PC_{71}BM$; thus, they can efficiently transfer electrons from the perovskite to the corresponding electrode.

As described in previous reports, lead atoms can not only readily coordinate with ligands through lead–oxygen interactions to form lead complexes[50−52] but also coordinate with the solvent (especially DMF and DMSO) through lead–oxygen interaction.[53,54] To probe the specific interfacial interactions between the perovskite and the fullerene layers, Fourier transform infrared (FTIR) spectra of the films of different components were recorded. The FTIR spectra of $PC_{61}BM$, $PC_{71}BM$, $DMEC_{60}$, $DMEC_{70}$, $PC_{61}BM$/perovskite, $DMEC_{60}$/perovskite, $PC_{71}BM$/perovskite, and $DMEC_{70}$/perovskite are shown in Figures S12–S14. The stretching C═O vibrations appear at 1736, 1749, 1736, and 1744 cm^{-1} for the pure $PC_{61}BM$, $DMEC_{60}$, $PC_{71}BM$, and $DMEC_{70}$, respectively, and these are shifted to 1732, 1741, 1733, and 1738 cm^{-1} for the corresponding perovskite composite. These shifts are attributed to the decrease in bond strength for C═O upon interfacial complexation. The stretching N–H vibrations appear at 3295 and 3293 cm^{-1} for the $DMEC_{60}$ and $DMEC_{70}$ films, respectively, and these are not observed after combining the compounds with the perovskite layers as $DMEC_{60}$/perovskite and $DMEC_{70}$/perovskite. Because similar phenomena have also been reported in previous articles,[55,56] we propose that the C═O peak shifts and N–H vibration disappearances can be attributed to specific interactions between the oxygen and nitrogen atoms on the fullerene derivatives with the lead atoms in the perovskites. These interfacial interactions between $DMEC_{60}$ (or $DMEC_{70}$) and the perovskite layers may effectively reduce charge recombination at the $DMEC_{60}$ (or

DOI: 10.1021/acsami.6b10668
ACS Appl. Mater. Interfaces 2016, 8, 31426–31432

$DMEC_{70}$)−perovskite interfaces and increase the electron extraction efficiencies from the perovskite to the fullerene layers.

To further probe the electron transporting property of $DMEC_{60}$ and $DMEC_{70}$ as ETMs, time-resolved photoluminescence (TRPL) spectra were measured. As shown in Figure 5, the films with perovskite/$DMEC_{60}$ (or $DMEC_{70}$)

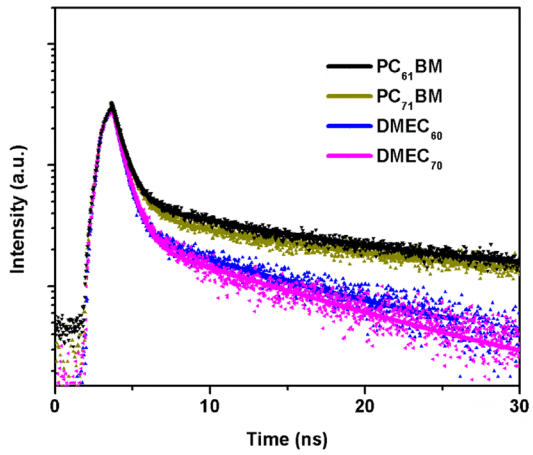

Figure 5. TRPL decay transient spectra of FTO/perovskite/$PC_{61}BM$, FTO/perovskite/$PC_{71}BM$, FTO/perovskite/$DMEC_{60}$, and FTO/perovskite/$DMEC_{70}$.

displayed shorter photoluminescence decay times of 6.3 ns (or 6.1 ns) compared to those of $PC_{61}BM$ (8.5 ns) or $PC_{71}BM$ (7.8 ns). This shorter photoluminescence decay time indicates that employing $DMEC_{60}$ or $DMEC_{70}$ as ETMs can enhance the electron extraction efficiency from the perovskite layer to the $DMEC_{60}$ (or $DMEC_{70}$) layer, thus leading to improved J_{sc} in $DMEC_{60}$- and $DMEC_{70}$-based PSCs.

Because the observation of hysteretic behavior in PSCs has become an important issue,[57] the hysteresis effects of the devices were measured. As shown in Figure S15, all the devices displayed relatively consistent $J-V$ curves regardless of the scan direction, indicating a negligible hysteresis effect in the PSCs with $PC_{61}BM$, $PC_{71}BM$, $DMEC_{60}$, or $DMEC_{70}$ as the ETMs. The results also indicate that the fullerene derivatives effectively reduce the charge traps at the fullerene−perovskite interface, which is consistent with previous reports.[58,59]

Meanwhile, to avoid overestimation of device efficiencies, the maximal steady-state power and photocurrent output were tested (Figure S16). $DMEC_{70}$- and $PC_{71}BM$-based cells lead to 20.6 and 19.0 mA cm^{-2} at 0.79 V, respectively, corresponding to PCEs of 16.3% and 15.0%. $DMEC_{60}$- and $PC_{61}BM$-based cells lead to 19.6 and 18.6 mA cm^{-2} at 0.77 V, respectively, corresponding to PCEs of 15.1% and 14.3%, which are very close to the values determined from the $J-V$ curves.

The stability of the devices with $DMEC_{60}$ and $DMEC_{70}$ as the ETMs were tested under AM 1.5 illumination in air. Because the LiF/Al electrode can be corroded upon air exposure and thereby potentially affect the device stability, the devices were encapsulated by mounting a glass sheet on top. As illustrated in Figure 6, the devices with $PC_{61}BM$ and $PC_{71}BM$ as the ETM lost ca. 60% of their performance after 10 days, while the devices with $DMEC_{60}$ and $DMEC_{70}$ kept more than 80% of their original performance. As shown in Figure S17, water droplets on perovskite/$PC_{61}BM$, perovskite/$PC_{71}BM$, perovskite/$DMEC_{60}$, and perovskite/$DMEC_{70}$ exhibit contact

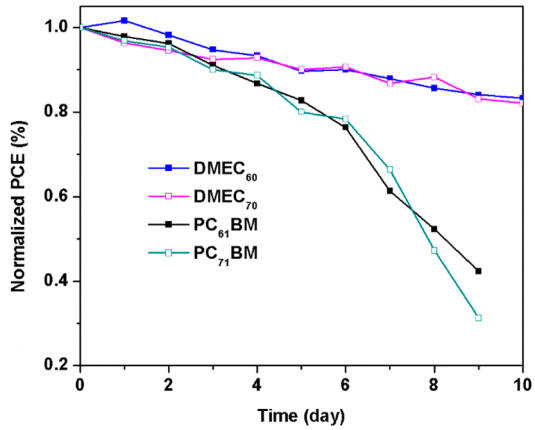

Figure 6. Normalized PCE of perovskite solar cells employing $PC_{61}BM$, $PC_{71}BM$, $DMEC_{60}$, and $DMEC_{70}$ ETMs as a function of storage time in air.

angles of 83°, 85°, 85° and 86°, respectively. These values show the wetting capability of the different substrate surfaces to water, and it appears that the pyrrolidine group on $DMEC_{60}$ and $DMEC_{70}$ make them slightly more hydrophobic than PCBMs. Another possible reason for the higher stability of the $DMEC_{60}$- or $DMEC_{70}$-based devices could be the result of the stronger adhesion and enhanced interfacial coupling between $DMEC_{60}$ (or $DMEC_{70}$) and the perovskite, preventing the Al from rapidly diffusing across the $DMEC_{60}$ ($DMEC_{70}$) layer into the perovskite layer. This phenomenon has been observed for devices employing a spiro-MeOTAD HTM and a Au or Ag back-contact.[60] These results also highlight the importance of the structure and composition of the attached group on the fullerene cage.

4. CONCLUSIONS

In conclusion, we designed and synthesized two ester-based fulleropyrrolidine derivatives, $DMEC_{60}$ and $DMEC_{70}$, as ETMs for PSCs. The devices based on $DMEC_{60}$ and $DMEC_{70}$ as ETMs yield PCEs up to 15.2% and 16.4%, respectively, which are higher than those measured for devices based on $PC_{61}BM$ (14.5%) and $PC_{71}BM$ (15.1%). The higher performance of the devices with $DMEC_{60}$ and $DMEC_{70}$ as the ETMs can be attributed not only to the suitable LUMO energy level and electron mobility but also to the ability to extract electrons efficiently, likely the result of specific interactions between the attached groups on the fullerene derivatives and the perovskite layers. The stability of the devices was improved when $DMEC_{60}$ and $DMEC_{70}$ are used as the ETMs. $DMEC_{60}$ and $DMEC_{70}$ are also convenient due to their much-easier synthesis and higher yield than those of $PC_{61}BM$ and $PC_{71}BM$. Therefore, these fullerene derivatives have the potential to become highly desirable alternatives in perovskite solar cells.

■ ASSOCIATED CONTENT

Supporting Information

The Supporting Information is available free of charge on the ACS Publications website at DOI: 10.1021/acsami.6b10668.

Detailed synthesis of the materials; ^{1}H NMR, ^{13}C NMR, MALDI-TOF, XRD, EQE spectra and device characterization; cyclic voltammetric curves; statistical diagrams; $J-V$ characteristics and curves; maximal steady-state photocurrent output; and images of water droplet

DOI: 10.1021/acsami.6b10668
ACS Appl. Mater. Interfaces 2016, 8, 31426−31432

contact angles. Additional FTIR characteristics. A table showing redox potentials. (PDF)

AUTHOR INFORMATION

Corresponding Author

*E-mail: echegoyen@utep.edu.

Author Contributions

§These authors contributed equally.

Notes

The authors declare no competing financial interest.

ACKNOWLEDGMENTS

L.E. thanks the US National Science Foundation (NSF) for generous support of this work under the NSF-PREM program (DMR 1205302). The Robert A. Welch Foundation is also gratefully acknowledged for an endowed chair to L.E. (grant AH-0033).

REFERENCES

(1) Kojima, A.; Teshima, K.; Shirai, Y.; Miyasaka, T. Organometal Halide Perovskites as Visible-Light Sensitizers for Photovoltaic Cells. *J. Am. Chem. Soc.* **2009**, *131*, 6050−6051.

(2) Wehrenfennig, C.; Eperon, G. E.; Johnston, M. B.; Snaith, H. J.; Herz, L. M. High Charge Carrier Mobilities and Lifetimes in Organolead Trihalide Perovskites. *Adv. Mater.* **2014**, *26*, 1584−1589.

(3) Xing, G.; Mathews, N.; Sun, S.; Lim, S. S.; Lam, Y. M.; Gratzel, M.; Mhaisalkar, S.; Sum, T. C. Long-Range Balanced Electron- and Hole-Transport Lengths in Organic-Inorganic $CH_3NH_3PbI_3$. *Science* **2013**, *342*, 344−347.

(4) Lee, M. M.; Teuscher, J.; Miyasaka, T.; Murakami, T. N.; Snaith, H. J. Efficient Hybrid Solar Cells Based on Meso-Superstructured Organometal Halide Perovskites. *Science* **2012**, *338*, 643−647.

(5) Stranks, S. D.; Eperon, G. E.; Grancini, G.; Menelaou, C.; Alcocer, M. J. P.; Leijtens, T.; Herz, L. M.; Petrozza, A.; Snaith, H. J. Electron-Hole Diffusion Lengths Exceeding 1 Micrometer in an Organometal Trihalide Perovskite Absorber. *Science* **2013**, *342*, 341−344.

(6) Im, J. H.; Lee, C. R.; Lee, J. W.; Park, S. W.; Park, N. G. 6.5% Efficient Perovskite Quantum-Dot-Sensitized Solar Cell. *Nanoscale* **2011**, *3*, 4088−4093.

(7) Kim, H. S.; Lee, C. R.; Im, J. H.; Lee, K. B.; Moehl, T.; Marchioro, A.; Moon, S. J.; Humphry-Baker, R.; Yum, J. H.; Moser, J. E.; Gratzel, M.; Park, N. G. Lead Iodide Perovskite Sensitized All-Solid-State Submicron Thin Film Mesoscopic Solar Cell with Efficiency Exceeding 9%. *Sci. Rep.* **2012**, *2*, 591−597.

(8) Liu, M. Z.; Johnston, M. B.; Snaith, H. J. Efficient Planar Heterojunction Perovskite Solar Cells by Vapour Deposition. *Nature* **2013**, *501*, 395−398.

(9) Zhou, H.; Chen, Q.; Li, G.; Luo, S.; Song, T. b.; Duan, H. S.; Hong, Z.; You, J.; Liu, Y.; Yang, Y. Interface Engineering of Highly Efficient Perovskite Solar Cells. *Science* **2014**, *345*, 542−546.

(10) Jeon, N. J.; Noh, J. H.; Yang, W. S.; Kim, Y. C.; Ryu, S.; Seo, J.; Seok, S. I. Compositional Engineering of Perovskite Materials for High-Performance Solar Cells. *Nature* **2015**, *517*, 476−480.

(11) Yang, W. S.; Noh, J. H.; Jeon, N. J.; Kim, Y. C.; Ryu, S.; Seo, J.; Seok, S. I. High-Performance Photovoltaic Perovskite Layers Fabricated through Intramolecular Exchange. *Science* **2015**, *348*, 1234−1237.

(12) Mei, A.; Li, X.; Liu, L.; Ku, Z.; Liu, T.; Rong, Y.; Xu, M.; Hu, M.; Chen, J.; Yang, Y.; Gratzel, M.; Han, H. A Hole-Conductor-Free, Fully Printable Mesoscopic Perovskite Solar Cell with High Stability. *Science* **2014**, *345*, 295−298.

(13) Bi, D.; Tress, W.; Dar, M. I.; Gao, P.; Luo, J.; Renevier, C.; Schenk, K.; Abate, A.; Giordano, F.; Correa Baena, J. P.; Decoppet, J. D.; Zakeeruddin, S. M.; Nazeeruddin, M. K.; Grätzel, M.; Hagfeldt, A. Efficient Luminescent Solar Cells Based on Tailored Mixed-Cation Perovskites. *Sci. Adv.* **2016**, *2*, E1501170.

(14) NREL Best Research-Cell Efficiencies. http://www.nrel.gov/pv/assets/images/efficiency_chart.jpg (accessed Sep 2016).

(15) Meng, L.; You, J.; Guo, T. F.; Yang, Y. Recent Advances in the Inverted Planar Structure of Perovskite Solar Cells. *Acc. Chem. Res.* **2016**, *49*, 155−165.

(16) Jeng, J. Y.; Chiang, Y. F.; Lee, M. H.; Peng, S. R.; Guo, T. F.; Chen, P.; Wen, T. C. $CH_3NH_3PbI_3$ Perovskite/Fullerene Planar-Heterojunction Hybrid Solar Cells. *Adv. Mater.* **2013**, *25*, 3727−3732.

(17) Docampo, P.; Ball, J. M.; Darwich, M.; Eperon, G. E.; Snaith, H. J. Efficient Organometal Trihalide Perovskite Planar-Heterojunction Solar Cells on Flexible Polymer Substrates. *Nat. Commun.* **2013**, *4*, 2761−2766.

(18) Jeng, J. Y.; Chen, K. C.; Chiang, T. Y.; Lin, P. Y.; Tsai, T. D.; Chang, Y. C.; Guo, T. F.; Chen, P.; Wen, T. C.; Hsu, Y. J. Nickel Oxide Electrode Interlayer in $CH_3NH_3PbI_3$ Perovskite/PCBM Planar-Heterojunction Hybrid Solar Cells. *Adv. Mater.* **2014**, *26*, 4107−4113.

(19) Kim, J. H.; Liang, P. W.; Williams, S. T.; Cho, N.; Chueh, C. C.; Glaz, M. S.; Ginger, D. S.; Jen, A. K. Y. High-Performance and Environmentally Stable Planar Heterojunction Perovskite Solar Cells Based on a Solution-Processed Copper-Doped Nickel Oxide Hole-Transporting Layer. *Adv. Mater.* **2015**, *27*, 695−701.

(20) Chen, W. Y.; Deng, L. L.; Dai, S. M.; Wang, X.; Tian, C. B.; Zhan, X. X.; Xie, S. Y.; Huang, R. B.; Zheng, L. S. Low-Cost Solution-Processed Copper Iodide as an Alternative to PEDOT:PSS Hole Transport Layer for Efficient and Stable Inverted Planar Heterojunction Perovskite Solar Cells. *J. Mater. Chem. A* **2015**, *3*, 19353−19359.

(21) Volker, S. F.; Collavini, S.; Delgado, J. L. Organic Charge Carriers for Perovskite Solar Cells. *ChemSusChem* **2015**, *8*, 3012−3028.

(22) Sun, S.; Salim, T.; Mathews, N.; Duchamp, M.; Boothroyd, C.; Xing, G.; Sum, T. C.; Lam, Y. M. The Origin of High Efficiency in Low-Temperature Solution-Processable Bilayer Organometal Halide Hybrid Solar Cells. *Energy Environ. Sci.* **2014**, *7*, 399−407.

(23) Nie, W.; Tsai, H.; Asadpour, R.; Blancon, J. C.; Neukirch, A. J.; Gupta, G.; Crochet, J. J.; Chhowalla, M.; Tretiak, S.; Alam, M. A.; Wang, H. L.; Mohite, A. D. High-Efficiency Solution-Processed Perovskite Solar Cells with Millimeter-Scale Grains. *Science* **2015**, *347*, 522−525.

(24) Heo, J. H.; Han, H. J.; Kim, D.; Ahn, T. K.; Im, S. H. Hysteresis-Less Inverted $CH_3NH_3PbI_3$ Planar Perovskite Hybrid Solar Cells with 18.1% Power Conversion Efficiency. *Energy Environ. Sci.* **2015**, *8*, 1602−1608.

(25) Chiang, C. H.; Tseng, Z. L.; Wu, C. G. Planar Heterojunction Perovskite/$PC_{71}BM$ Solar Cells with Enhanced Open-Circuit Voltage via a (2/1)-Step Spin-Coating Process. *J. Mater. Chem. A* **2014**, *2*, 15897−15903.

(26) Kim, J. H.; Williams, S. T.; Cho, N.; Chueh, C. C.; Jen, A. K. Y. Enhanced Environmental Stability of Planar Heterojunction Perovskite Solar Cells Based on Blade-Coating. *Adv. Energy Mater.* **2015**, *5*, 1401229.

(27) Liang, P. W.; Chueh, C. C.; Williams, S. T.; Jen, A. K. Y. Roles of Fullerene-Based Interlayers in Enhancing the Performance of Organometal Perovskite Thin-Film Solar Cells. *Adv. Energy Mater.* **2015**, *5*, 1402321.

(28) Azimi, H.; Ameri, T.; Zhang, H.; Hou, Y.; Quiroz, C. O. R.; Min, J.; Hu, M.; Zhang, Z. G.; Przybilla, T.; Matt, G. J.; Spiecker, E.; Li, Y.; Brabec, C. J. A Universal Interface Layer Based on an Amine-Functionalized Fullerene Derivative with Dual Functionality for Efficient Solution Processed Organic and Perovskite Solar Cells. *Adv. Energy Mater.* **2015**, *5*, 1401692.

(29) Xiao, Z.; Bi, C.; Shao, Y.; Dong, Q.; Wang, Q.; Yuan, Y.; Wang, C.; Gao, Y.; Huang, J. Efficient, High Yield Perovskite Photovoltaic Devices Grown by Interdiffusion of Solution-Processed Precursor Stacking Layers. *Energy Environ. Sci.* **2014**, *7*, 2619−2623.

(30) Wang, Q.; Shao, Y.; Dong, Q.; Xiao, Z.; Yuan, Y.; Huang, J. Large Fill-Factor Bilayer Iodine Perovskite Solar Cells Fabricated by a

DOI: 10.1021/acsami.6b10668
ACS Appl. Mater. Interfaces 2016, 8, 31426−31432

Low-Temperature Solution-Process. *Energy Environ. Sci.* **2014**, *7*, 2359−2365.
(31) Liu, X.; Jiao, W.; Lei, M.; Zhou, Y.; Song, B.; Li, Y. Crown-Ether Functionalized Fullerene as a Solution-Processable Cathode Buffer Layer for High Performance Perovskite and Polymer Solar Cells. *J. Mater. Chem. A* **2015**, *3*, 9278−9284.
(32) Shao, Y.; Yuan, Y.; Huang, J. Correlation of Energy Disorder and Open-Circuit Voltage in Hybrid Perovskite Solar Cells. *Nat. Energy* **2016**, *1*, 15001.
(33) Zhang, H.; Azimi, H.; Hou, Y.; Ameri, T.; Przybilla, T.; Spiecker, E.; Kraft, M.; Scherf, U.; Brabec, C. J. Improved High-Efficiency Perovskite Planar Heterojunction Solar Cells via Incorporation of a Polyelectrolyte Interlayer. *Chem. Mater.* **2014**, *26*, 5190−5193.
(34) Xie, F. X.; Zhang, D.; Su, H.; Ren, X.; Wong, K. S.; Grätzel, M.; Choy, W. C. H. Vacuum-Assisted Thermal Annealing of $CH_3NH_3PbI_3$ for Highly Stable and Efficient Perovskite Solar Cells. *ACS Nano* **2015**, *9*, 639−646.
(35) Xue, Q.; Hu, Z.; Liu, J.; Lin, J.; Sun, C.; Chen, Z.; Duan, C.; Wang, J.; Liao, C.; Lau, W. M.; Huang, F.; Yip, H.-L.; Cao, Y. Highly Efficient Fullerene/Perovskite Planar Heterojunction Solar Cells via Cathode Modification with an Amino-Functionalized Polymer Interlayer. *J. Mater. Chem. A* **2014**, *2*, 19598−19603.
(36) Li, C.; Wang, F.; Xu, J.; Yao, J.; Zhang, B.; Zhang, C.; Xiao, M.; Dai, S.; Li, Y.; Tan, Z. a., Efficient Perovskite/Fullerene Planar Heterojunction Solar Cells with Enhanced Charge Extraction and Suppressed Charge Recombination. *Nanoscale* **2015**, *7*, 9771−9778.
(37) Zhang, X.; Gan, L.; Huang, S.; Shi, Y. Iodo-Controlled Selective Formation of Pyrrolidino[60]Fullerene and Aziridino[60]Fullerene from the Reaction between C_{60} and Amino Acid Esters. *J. Org. Chem.* **2004**, *69*, 5800−5802.
(38) Sun, Q. J.; Wang, H. Q.; Yang, C. H.; Li, Y. F. Synthesis and Electroluminescence of Novel Copolymers Containing Crown Ether Spacers. *J. Mater. Chem.* **2003**, *13*, 800−806.
(39) Hummelen, J. C.; Knight, B. W.; Lepeq, F.; Wudl, F.; Yao, J.; Wilkins, C. L. Preparation and Characterization of Fulleroid and Methanofullerene Derivatives. *J. Org. Chem.* **1995**, *60*, 532−538.
(40) Ishii, H.; Sugiyama, K.; Ito, E.; Seki, K. Energy Level Alignment and Interfacial Electronic Structures at Organic/Metal and Organic/Organic Interfaces. *Adv. Mater.* **1999**, *11*, 605−625.
(41) Cahen, D.; Kahn, A. Electron Energetics at Surfaces and Interfaces: Concepts and Experiments. *Adv. Mater.* **2003**, *15*, 271−277.
(42) Murgatroyd, P. N. Theory of Space-Charge-Limited Current Enhanced by Frenkel Effect. *J. Phys. D: Appl. Phys.* **1970**, *3*, 151−156.
(43) Leijtens, T.; Lim, J.; Teuscher, J.; Park, T.; Snaith, H. J. Charge Density Dependent Mobility of Organic Hole-Transporters and Mesoporous TiO2 Determined by Transient Mobility Spectroscopy: Implications to Dye-Sensitized and Organic Solar Cells. *Adv. Mater.* **2013**, *25*, 3227−3233.
(44) Li, Y.; Zhao, Y.; Chen, Q.; Yang, Y.; Liu, Y.; Hong, Z.; Liu, Z.; Hsieh, Y. T.; Meng, L.; Li, Y.; Yang, Y. Multifunctional Fullerene Derivative for Interface Engineering in Perovskite Solar Cells. *J. Am. Chem. Soc.* **2015**, *137*, 15540−15547.
(45) Chen, Q.; Zhou, H.; Hong, Z.; Luo, S.; Duan, H. S.; Wang, H. H.; Liu, Y.; Li, G.; Yang, Y. Planar Heterojunction Perovskite Solar Cells via Vapor Assisted Solution Process. *J. Am. Chem. Soc.* **2014**, *136*, 622−625.
(46) Burschka, J.; Pellet, N.; Moon, S. J.; Humphry-Baker, R.; Gao, P.; Nazeeruddin, M. K.; Grätzel, M. Sequential Deposition as a Route to High-Performance Perovskite-Sensitized Solar Sells. *Nature* **2013**, *499*, 316−319.
(47) Liang, K.; Mitzi, D. B.; Prikas, M. T. Synthesis and Characterization of Organic-Inorganic Perovskite Thin Films Prepared Using a Versatile Two-Step Dipping Technique. *Chem. Mater.* **1998**, *10*, 403−411.
(48) Jeon, N. J.; Noh, J. H.; Kim, Y. C.; Yang, W. S.; Ryu, S.; Seok, S. I. Solvent Engineering for High-Performance Inorganic-Organic Hybrid Perovskite Solar Cells. *Nat. Mater.* **2014**, *13*, 897−903.
(49) Yang, G.; Tao, H.; Qin, P.; Ke, W.; Fang, G. Recent Progress in Electron Transport Layers for Efficient Perovskite Solar Cells. *J. Mater. Chem. A* **2016**, *4*, 3970−3990.
(50) Mahmoudi, G.; Bauzá, A.; Frontera, A. Concurrent Agostic and Tetrel Bonding Interactions in Lead(II) Complexes with an Isonicotinohydrazide Based Ligand and Several Anions. *Dalton Trans.* **2016**, *45*, 4965−4969.
(51) Davidovich, R. L.; Stavila, V.; Marinin, D. V.; Voit, E. I.; Whitmire, K. H. Stereochemistry of Lead(II) Complexes with Oxygen Donor Ligands. *Coord. Chem. Rev.* **2009**, *253*, 1316−1352.
(52) Lyczko, K.; Narbutt, J.; Paluchowska, B.; Maurin, J. K.; Persson, I. Crystal Structure of Lead(II) Acetylacetonate and the Structure of the Acetylacetone Solvated Lead(II) Ion in Solution Studied by Large-Angle X-ray Scattering. *Dalton Trans.* **2006**, *33*, 3972−3976.
(53) Wakamiya, A.; Endo, M.; Sasamori, T.; Tokitoh, N.; Ogomi, Y.; Hayase, S.; Murata, Y. Reproducible Fabrication of Efficient Perovskite-based Solar Cells: X-ray Crystallographic Studies on the Formation of $CH_3NH_3PbI_3$ Layers. *Chem. Lett.* **2014**, *43*, 711−713.
(54) Guo, Y.; Shoyama, K.; Sato, W.; Matsuo, Y.; Inoue, K.; Harano, K.; Liu, C.; Tanaka, H.; Nakamura, E. Chemical Pathways Connecting Lead(II) Iodide and Perovskite via Polymeric Plumbate(II) Fiber. *J. Am. Chem. Soc.* **2015**, *137*, 15907−15914.
(55) Saliba, M.; Orlandi, S.; Matsui, T.; Aghazada, S.; Cavazzini, M.; Correa-Baena, J. P.; Gao, P.; Scopelliti, R.; Mosconi, E.; Dahmen, K. H.; De Angelis, F.; Abate, A.; Hagfeldt, A.; Pozzi, G.; Graetzel, M.; Nazeeruddin, M. K. A Molecularly Engineered Hole-Transporting Material for Efficient Perovskite Solar Cells. *Nat. Energy* **2016**, *1*, 15017.
(56) Cao, J.; Liu, Y.-M.; Jing, X.; Yin, J.; Li, J.; Xu, B.; Tan, Y. Z.; Zheng, N. Well-Defined Thiolated Nanographene as Hole-Transporting Material for Efficient and Stable Perovskite Solar Cells. *J. Am. Chem. Soc.* **2015**, *137*, 10914−10917.
(57) Chen, B.; Yang, M.; Priya, S.; Zhu, K. Origin of *J*−*V* Hysteresis in Perovskite Solar Cells. *J. Phys. Chem. Lett.* **2016**, *7*, 905−917.
(58) Shao, Y.; Xiao, Z.; Bi, C.; Yuan, Y.; Huang, J. Origin and Elimination of Photocurrent Hysteresis by Fullerene Passivation in $CH_3NH_3PbI_3$ Planar Heterojunction Solar Cells. *Nat. Commun.* **2014**, *5*, 5784.
(59) Xu, J.; Buin, A.; Ip, A. H.; Li, W.; Voznyy, O.; Comin, R.; Yuan, M.; Jeon, S.; Ning, Z.; McDowell, J. J.; Kanjanaboos, P.; Sun, J.-P.; Lan, X.; Quan, L. N.; Kim, D. H.; Hill, I. G.; Maksymovych, P.; Sargent, E. H. Perovskite-Fullerene Hybrid Materials Suppress Hysteresis in Planar Diodes. *Nat. Commun.* **2015**, *6*, 7801.
(60) Domanski, K.; Correa-Baena, J.-P.; Mine, N.; Nazeeruddin, M. K.; Abate, A.; Saliba, M.; Tress, W.; Hagfeldt, A.; Grätzel, M. Not All That Glitters Is Gold: Metal-Migration-Induced Degradation in Perovskite Solar Cells. *ACS Nano* **2016**, *10*, 6306−6314.

DOI: 10.1021/acsami.6b10668
ACS Appl. Mater. Interfaces 2016, 8, 31426−31432